THE JOURNAL OF PHYSICAL CHEMISTRY C

Article

pubs.acs.org/JPCC

Mechanisms of the Oxygen Reduction Reaction on Defective Graphene-Supported Pt Nanoparticles from First-Principles

Dong-Hee Lim and Jennifer Wilcox*

Department of Energy Resources Engineering, Stanford University, 367 Panama Street, Green Earth Sciences, Stanford, California 94305-2220

Supporting Information

ABSTRACT: The mechanisms of the oxygen reduction reaction (ORR) on defective graphene-supported Pt_{13} nanoparticles have been investigated to understand the effect of defective graphene support on the ORR and predict details of ORR pathways. We employed density functional theory (DFT) predictions using the projector-augmented wave (PAW) method within the generalized gradient approximation (GGA). Free energy diagrams for the ORR over supported and unsupported Pt_{13} nanoparticles were constructed to provide the stability of possible intermediates in the electrochemical reaction pathways. We demonstrate that the defective graphene support may provide a balance in the binding of ORR intermediates on Pt_{13} nanoparticles by tuning the relatively high reactivity of free Pt_{13} nanoparticles that bind the ORR intermediates too strongly subsequently leading to slow kinetics. The defective graphene support lowers not only the activation energy for O_2 dissociation from 0.37 to 0.16 eV, but also the energy barrier of the rate-limiting step by reducing the stability of HO* species. We predict the ORR mechanisms via direct four-electron and series two-electron pathways. It has been determined that an activation free energy (0.16 eV) for O_2 dissociation from adsorbed O_2* at a bridge site on the supported Pt_{13} nanoparticle into O* + O* species (i.e., the direct pathway) is lower than the free energy barrier (0.29 eV) for the formation of HOO* species from adsorbed O_2* at the corresponding atop site, indicating that the direct pathway may be preferred as the initial step of the ORR mechanism. Also, it has been observed that charge is transferred from the Pt_{13} nanoparticle to both defective graphene and the ORR intermediate species.

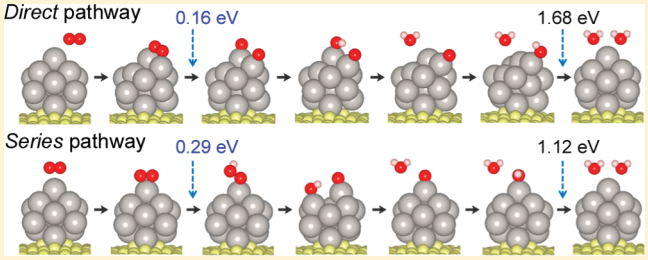

1. INTRODUCTION

The oxygen reduction reaction (ORR) is of central focus amidst ongoing studies of electrode reactions in polymer electrolyte membrane (PEM) fuel cells because of the slow kinetics that take place at the cathode electrode. Although efforts are being pursued to try and advance its performance to achieve improved efficiency,[1−4] the slow kinetics of the ORR limits PEM fuel cell applications. Platinum (Pt) has been reported as one of the best electrocatalysts for PEM fuel cells; however, its high cost is one of the main obstacles to the commercialization of PEM fuel cells.[5,6] For this Pt and Pt alloy nanocatalysts supported on graphene,[7−11] graphene nanoplatelets,[12] or nanoscale graphite[13] have gained much attention because of the reduction in the high cost of the precious metal and the increase in the durability of the Pt support. In particular, functionalized graphene-supported Pt nanoparticles show enhanced oxygen reduction activity in a PEM fuel cell,[7] better performance in a hydrogen fuel cell,[8] and also higher activity for methanol oxidation reaction[11] because of increased electrochemically active surface area and less aggregation of Pt nanoparticles. Furthermore, the vacancy sites in graphene can serve as anchoring points for the growth of nanoparticles.[14,15] Defective graphene-supported nanoparticles may enhance surface reactivity[14,16] and previous experimental studies have shown that atomic defects in graphene may be formed after several tens of seconds of irradiation with an electron beam[17] or by treatment with hydrochloric acid.[18]

The mechanisms of the ORR have been investigated experimentally and theoretically for Pt and Pt alloy catalysts. The following two overall mechanisms of ORR have been suggested:[1,19] a direct four-electron pathway (eq 1), in which O_2 is directly reduced to H_2O without the formation of the hydrogen peroxide (H_2O_2) intermediate and a series two-electron pathway (eqs 2 and 3) in which O_2 is reduced to H_2O via H_2O_2.

$$O_2 + 4(H^+ + e^-) \rightarrow 2H_2O \quad (1)$$

$$O_2 + 2(H^+ + e^-) \rightarrow H_2O_2 \quad (2)$$

$$H_2O_2 + 2(H^+ + e^-) \rightarrow 2H_2O \quad (3)$$

It has been reported that the ORR proceeds principally through the direct pathway in both acid and alkaline aqueous electrolytes, provided that adsorbed impurities are minimal.[1] However, Markovic et al.[20] suggested that the series pathway may apply to Pt- and Pt-based bimetallic catalysts. In place of one dominant mechanism of either a direct or a series pathway, a parallel

Received: November 9, 2011
Revised: January 6, 2012
Published: January 11, 2012

pathway has also been suggested in which both the direct and series pathways take place simultaneously,[21] with the direct pathway dominant.[3,22]

The ORR pathway may also be influenced by the adsorption and coverage of oxygen on the Pt surface. Nørskov et al.[2] reported that an associative mechanism is dominant at high oxygen coverage (θ_O = 0.5 monolayer (ML)), in which ORR occurs via the formation of an HOO* intermediate (i.e., the series pathway). While a dissociative mechanism is dominant at low oxygen coverage (θ_O = 0 ML) in which ORR occurs without the formation of an HOO* intermediate (i.e., the direct pathway). Yeager[23] postulated that the direct pathway occurs when O_2 molecule is adsorbed as a di-σ structure (i.e., a bridge site-configuration), while the series pathway is preferred when only one atomic site is available (i.e., an atop site-configuration). On the other hand, Sidik and Anderson[24] conducted a DFT cluster study and showed that O_2 bonded to a dual site on a Pt_2 cluster proceeds via the series pathway, not being dissociated, but through the formation of an HOO* species

Despite efforts ongoing theoretical investigations of ORR mechanisms on flat Pt and Pt alloy metals as previously discussed, few theoretical studies of ORR mechanisms on graphene-supported Pt nanoparticles have been conducted to date. The purpose of the current study is to investigate ORR mechanisms on defective graphene−supported Pt nanoparticles using density functional theory (DFT) calculations coupled with a computational hydrogen model (CHE)[2] to provide information regarding the stability of possible intermediates within the electrochemical reaction pathways. Although metal nanoparticles used for the ORR applications are deposited on various substrates (e.g., usually carbon supports),[25,26] we compare our O_2 adsorption and reactivity results to free Pt_{13} nanoparticles to demonstrate the effect of a defective graphene support on the catalytic activity of Pt_{13} nanoparticles. In addition, details of the structural and electronic properties of these systems are discussed.

2. COMPUTATIONAL METHODOLOGY

Spin-polarized density functional theory calculations were performed using the Vienna ab initio Simulation Package (VASP)[27−30] with the projector-augmented wave (PAW)[31,32] method. Electron exchange-correlation functionals were represented with the generalized gradient approximation (GGA), and the model of Perdew, Burke and Ernzerhof (PBE)[33] was used for the non-local corrections. An orthorhombic supercell of 19.74 × 17.10 × 32.01 Å with periodic boundary conditions was used with a vacuum space of 25.5 Å. A dipole moment correction was not incorporated due to its negligible effect on adsorption energy of Fe_{13} nanoparticle on a monovacancy defective graphene.[14] A kinetic energy cutoff of 400 eV was used with a plane-wave basis set. The integration of the Brillouin zone was conducted using a 2 × 2 × 1 Monkhorst−Pack grid[34] with the Γ-point included and first-order Methfessel−Paxton smearing[35] with a width of 0.1 eV. All atoms were fully relaxed and optimized until total energy change upon two steps of the electronic self-consistent loop less than 10^{-4} eV.

The supercell used for a monovacancy defective graphene consists of 127 carbon atoms with a single carbon atom vacancy at the center. A Pt_{13} cluster was chosen for a Pt nanoparticle according to "magic numbers" n[36,37] of transition-metal clusters (Fe, Ti, Zr, Nb, and Ta), such that, n = 7, 13, and 15 atoms that provide a higher geometric or electronic stability than other cluster sizes. The isolated Pt_{13} nanoparticle was optimized in a 25.0 Å cubic supercell, in which the Brillouin zone integration was carried out for the Γ-point only. Oxygen adsorbates on Pt_{13} surfaces were considered as neutrally charged oxygen adsorbates, instead of superoxide O_2^- or peroxide O_2^{2-}, as studied by Nørskov et al.[2] showing reasonable agreement with experiments in terms of ORR overpotential calculations (more details in Supporting Information, Computational Methodology section 1). The adsorption energy (E_{ads}) of an adsorbate (O_2) is defined as $E_{ads} = E_{substrate+adsorbate} - E_{substrate} - E_{adsorbate}$, where $E_{substrate+adsorbate}$, $E_{substrate}$, and $E_{adsorbate}$ are the total energies of a substrate and adsorbate (O_2−Pt_{13}-defective graphene), a substrate (Pt_{13}-defective graphene), and a gas phase adsorbate (O_2). A negative adsorption energy indicates that adsorption is exothermic (stable) with respect to the free gas phase adsorbate. More details of the adsorption of Pt_{13} nanoparticles on defective graphene and the adsorption of O_2 on Pt_{13}-defective graphene are discussed in our previous study.[15]

Fully relaxed and optimized Pt_{13}-defective graphene systems were partially frozen for this ORR study to save computational effort. The boundary 83 carbon atoms out of 127 carbon atoms of defective graphene were frozen based on its negligible influence on O_2 adsorption and geometry change as shown in Supporting Information, Computational Methodology section 2 (Figure S1 and Figure S2). The change in O_2 adsorption energies used for the ORR mechanism pathways is less than 5 meV because of the frozen carbon atoms. The activation barriers of O_2 dissociation are computed using the climbing image nudged elastic band (CI-NEB) method that is known to effectively locate the minimum energy paths (MEPs) and the corresponding transition states of adsorbate molecules on the transition metal surface.[38] Once the initial and final configurations of a reaction path are known, intermediate configurations are determined by interpolating between the initial and final configurations. The interpolated chain of configurations are connected by springs and relaxed simultaneously to the MEP, through which the highest-energy configuration climbs uphill to the saddle point.[38]

Free energies of the ORR intermediates in electrochemical reaction pathways were calculated based on a computational hydrogen electrode (CHE) model suggested by Nørskov et al.[2,39,40] The CHE model defines that the chemical potential of a proton/electron ($H^+ + e^-$) in solution is equal to half of the chemical potential of a gas-phase H_2. Free energy change (ΔG) is calculated as $\Delta G = \Delta E + \Delta ZPE - T\Delta S$, where ΔE is the total energy change directly obtained from DFT calculations, ΔZPE is the change in zero-point energies, T is temperature (298.15 K), and ΔS is the change in entropy. The effect of a bias can be applied by shifting ΔG by $-eU$, where e is the elementary positive charge and U is the applied bias. Free energies of adsorbates were calculated by treating $3N$ degrees of freedom of adsorbates as vibrational frequencies in the harmonic oscillator approximation and fixing Pt_{13}-defective graphene surfaces (assuming vibrations of the Pt_{13}-defective graphene surfaces are negligible) as done in Peterson et al.[40] Zero-point energies and entropies of the ORR intermediates were calculated from the vibrational frequencies according to standard methods,[41] and those of free gas-phase molecules were obtained from thermodynamics database.[2] Details of free energy calculations and DFT total energies, ZPE, entropies, and free energies of the intermediates are shown in Supporting Information, Computational Methodology section 3 (Table S1).

The Bader charge analysis[42−44] was carried out for the optimized geometries of free O_2, Pt_{13}-defective graphene, and O_2−Pt_{13}-defective graphene to quantitatively compare transferred

dx.doi.org/10.1021/jp210796e | J. Phys. Chem. C 2012, 116, 3653−3660

charges among O_2, Pt_{13} nanoparticle, and defective graphene. The charge difference density ($\Delta n(\mathbf{r})$) plot of the HOO–Pt_{13}-defective graphene system upon HOO adsorption was obtained by subtracting the charge densities of the separated constitutes of the HOO adsorbate ($n(\mathbf{r})_{adsorbate}$) and Pt_{13}-defective graphene substrate ($n(\mathbf{r})_{substrate}$) from the charge density of the HOO–Pt_{13}-defective graphene system ($n(\mathbf{r})_{system}$) as $n(\mathbf{r})_{system} - [n(\mathbf{r})_{adsorbate} + n(\mathbf{r})_{substrate}]$. The source of the isolated HOO and Pt_{13}-defective graphene structures have been directly obtained from the optimized structure of the O_2 adsorbed Pt_{13}-defective graphene system.

3. RESULTS AND DISCUSSION

Simple Oxygen Reduction over Pt_{13} Nanoparticle. A simple model for ORR, in which one atomic oxygen adsorbs on the surface (O*, asterisk denoting adsorbed species thereafter) and undergoes the first and second proton/electron ($H^+ + e^-$)-transfer steps (HO* and H_2O, respectively), is useful in providing insight on the activity of the Pt_{13} nanoparticle compared to that of flat Pt metals. Figure 1 shows the free energy diagrams

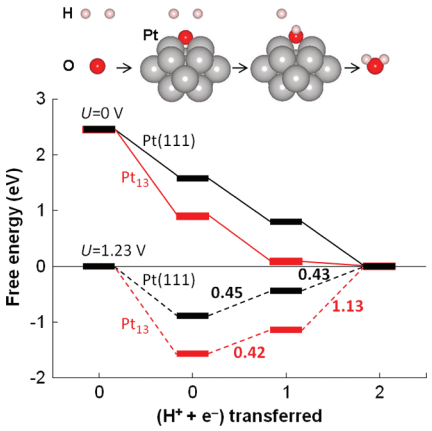

Figure 1. Free energy diagram for the simple oxygen reduction model over a Pt_{13} nanoparticle (red) compared to that of Pt(111) (black) by Nørskov et al.[2] Solid and dashed lines represent reactions at zero cell potential (U = 0 V) and the equilibrium potential (U = 1.23 V), respectively.

of the simple ORR over the Pt_{13} nanoparticle compared to that of Pt(111)[2], illustrating the four reaction steps with optimized intermediates, O* and HO*. At zero electrode potential (U = 0 V), roughly equivalent to the gas-phase hydrogen oxidation reaction,[2] both the Pt_{13} nanoparticle and Pt(111) exhibit exothermic reactivity. At an equilibrium electrode potential of U = 1.23 V, that is, the maximum thermodynamic potential of the fuel cell,[2] both materials exhibit energetically uphill proton/electron-transfer steps. Nørskov et al.[2] have suggested that the origin of the overpotential for ORR at the Pt cathode is attributed to one of two energetically uphill steps (0.45 eV), which is close to the experimentally measured overpotential. In the case of the Pt_{13} nanoparticle, the O* and HO* species are strongly stabilized, with adsorption energies of −4.99 and −3.54 eV, respectively. These adsorption energies are significantly stronger than those of O* on Pt(111) (i.e., −4.21 eV[45]) and HO* on Pt(111) (i.e., −2.25[46] or −2.31 eV[47]). The greater stability of these intermediates promotes the initial oxygen binding step on the Pt_{13} nanoparticle; however, it may hinder further reaction steps toward oxygen reduction due to potentially increased energy barriers associated with the proton/electron-transfer steps. The binding of HO* on the Pt_{13} nanoparticle is relatively stronger compared to the O* binding. The rate-limiting step lies in the second proton/electron-transfer step with an overpotential of 1.13 eV (i.e., defined as the minimum energy required for total process[2]) as shown in Figure 1. This strong binding interaction of the O* and HO* intermediates with the free Pt_{13} surface may cause the proton/electron-transfer steps to be strongly endothermic, thereby thermodynamically hindering the formation of product species.

In addition to investigation of the bridge site for ORR intermediate adsorption, less stable configurations of the atop site were also examined and are available in Supporting Information, Figure S3. The adsorption energies of O* and HO* on the atop site are −4.72 and −3.42 eV, respectively, which are 0.27 and 0.12 eV higher than those of the intermediates at the bridge site, resulting in minimum energy barriers for the first and second reduction steps of 0.25 and 1.05 eV, respectively. This result also indicates that an ORR pathway involving stronger binding of O* and HO* intermediates requires higher overpotentials for oxygen reduction.

Direct Pathway of ORR on Pt_{13}-Defective Graphene. Similarly, in the simple ORR pathway, a direct four-electron pathway of ORR on defective graphene-supported Pt_{13} nanoparticles has been investigated according to the following reaction steps:

$$O_2 \rightarrow O_2^* \quad (4)$$

$$O_2^* \rightarrow O^* + O^* \quad (5)$$

$$O^* + O^* + (H^+ + e^-) \rightarrow O^* + OH^* \quad (6)$$

$$O^* + OH^* + (H^+ + e^-) \rightarrow O^* + H_2O \quad (7)$$

$$O^* + H_2O + (H^+ + e^-) \rightarrow OH^* + H_2O \quad (8)$$

$$OH^* + H_2O + (H^+ + e^-) \rightarrow 2H_2O \quad (9)$$

The O_2 adsorption configurations on the Pt_{13}-defective graphene systems have been extensively investigated in our previous study,[15] in which it was found that O_2 prefers to bind on the Pt_{13}-defective graphene systems in a bridge configuration with an adsorption energy of −2.30 eV. This bridge configuration (i.e., a di-σ structure in which O_2 adsorbs over two Pt atoms) is likely to proceed toward oxygen reduction via the direct pathway[23] and may involve O_2 dissociation rather than the formation of HOO* intermediate species by protonation.[2] However, it is still unclear whether O_2 dissociation occurs prior to proton/electron-transfer steps. To investigate this, we tested the adsorption of atomic hydrogen on O_2 adsorbed in the bridge configuration as shown in Figure 2A. The geometry optimization indicates that upon H adsorption, the O–O bond dissociates and O* and HO* species are formed (Figure 2A). Thus, we postulate that O_2 dissociates at the bridge O_2 adsorption configuration and proceeds to further proton/electron-transfer steps as described in eqs 4–9 and steps 1–7 in Figure 3. The same direct pathway of ORR is also investigated on the free Pt_{13} nanoparticle to understand the effect of the defective graphene support on ORR mechanisms.

Figure 3 shows a comparison of the ORR mechanisms between the Pt_{13}-defective graphene and the free Pt_{13} nanoparticle. At zero electrode potential (U = 0 V), both show strong exothermicities except for the last step associated with H_2O desorption. This endothermic step (i.e., steps 6 → 7) is due to the exceptional stability of HO* at step 6 on both

dx.doi.org/10.1021/jp210796e | J. Phys. Chem. C 2012, 116, 3653–3660

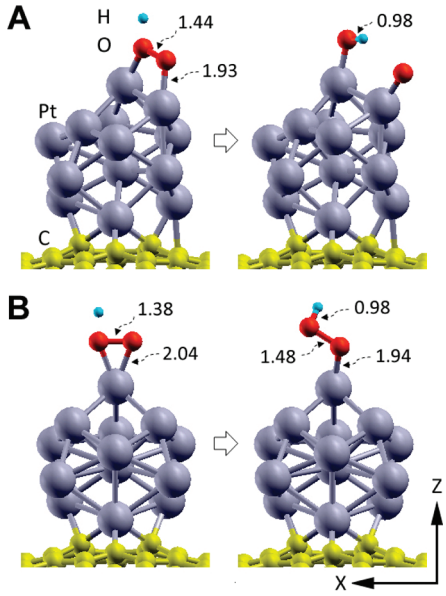

Figure 2. Geometry optimization of atomic hydrogen adsorption at bridge (A) and atop (B) sites on O_2–Pt_{13}-defective graphene systems. Optimized O_2^* adsorption configurations and initial positions of H atoms are in the left side and optimized H atoms are in the right side. Numbers with arrows represent bond lengths in Å.

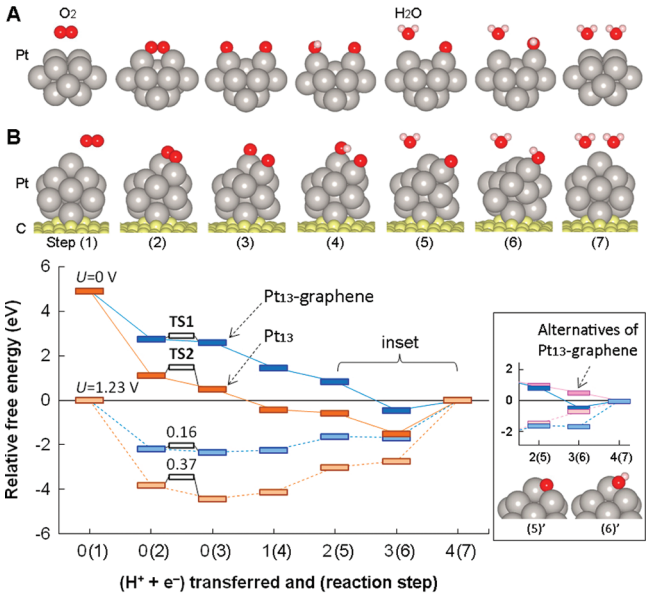

Figure 3. Free-energy diagram for oxygen reduction through a direct four-electron pathway on free Pt_{13} nanoparticles (**A** and markers in orange) and defective graphene-supported Pt_{13} nanoparticles (**B** and markers in blue). Solid and dashed lines represent reactions at zero cell potential (i.e., U = 0 V) and the equilibrium potential (i.e., U = 1.23 V), respectively. Images of steps 1–7 correspond to eqs 4–9 (a direct four-electron pathway). Gas-phase species (e.g., O_2, H_2O, and H_2) are separately calculated and protons in the gas-phase are omitted in the images. TS 1 and 2 represent activation free energies for O_2 dissociation on the supported and unsupported Pt_{13} nanoparticles, respectively. Inset shows alternative intermediates (less stable) of step 5′ and 6′ of the supported Pt_{13} system.

supported and unsupported Pt_{13} nanoparticles. In contrast to the strongly bound O* and HO* intermediates on the atop site of the Pt_{13}-defective graphene at steps 5 and 6, respectively, the less stable intermediates of these steps lead to exothermic reactions as shown in the inset. The adsorption behavior of OH on the Pt_{13}-defective graphene agrees with that of OH on Pt(111) in that OH prefers to bind at an atop site rather than a bridge site.[46,47] For the supported system, at the equilibrium electrode potential (i.e., U = 1.23 V), all of the four proton/electron-transfer steps are energetically uphill (endothermic reactions) except for step 5 → 6. The rate-limiting steps lie in the last proton/electron transfer and H_2O desorption steps (i.e., step 6 → 7), with minimum energy barriers of 1.68 and 2.71 eV for both supported and unsupported Pt_{13} nanoparticles, respectively. In the case of the less stable intermediates of the supported system shown in the inset of Figure 3, the rate-limiting step appears at the second proton/electron transfer and first H_2O desorption step (i.e., step 4 → 5) with a minimum energy barrier of 0.78 eV. This remarkable change in the rate-limiting energy barrier indicates that the stability of the ORR intermediates, that is, O* and HO*, serves a key role in the activity of Pt surfaces toward oxygen reduction as previously discussed. In addition, the defective graphene support significantly contributes to the reduction of the energy barrier, which provides an opportunity for tuning the activity of Pt nanoparticles using the graphene support. The decrease in the stability of the ORR intermediates may be due to a charge redistribution caused by the defective graphene support. Upon O_2 adsorption on the Pt_{13}-defective graphene, charge flows from the Pt_{13} nanoparticle to both O_2 and defective graphene as shown in our previous study.[15]

Free energies of activation for O_2 dissociation (between steps 2 → 3) on both supported (TS1) and unsupported Pt_{13} (TS2) nanoparticles are 0.16 and 0.37 eV, respectively, as shown in Figure 3. The defective graphene support significantly lowers the O_2 dissociation barrier compared to the energy barriers of the free Pt_{13} nanoparticle and flat Pt surfaces, which range in DFT gas-phase calculations between 0.24 and 0.76 eV depending on O_2 coverage (e.g., 0.12–0.50 ML) on Pt(111),[48] 0.69 and 0.90 eV on Pt(111),[49] 0.8 and 0.9 eV on Pt(211),[49] 0.44 eV on Pt(111),[50] and between 0.15 and 0.30 eV on Pt(111).[51] The O_2 dissociation barrier energy on the free Pt_{13} nanoparticle is close to the experimental value of 0.32 eV on Pt(111) in the gas-phase.

The lower O_2 dissociation barrier of the Pt_{13}-defective graphene system compared to the free Pt_{13} nanoparticle is directly associated with the degree of activation of the adsorbed O_2 molecule at the bridge site of the Pt_{13} nanoparticles. Comparing the O–O bond lengths on both systems as shown in Table 1 and Figure 2, the O–O bond distance of 1.44 Å on the Pt_{13}-defective graphene is more elongated than that of the free Pt_{13} nanoparticle (1.40 Å). The elongated O–O bond length is consistent with the O_2 excess Bader charges (i.e., charge transferred to O_2) of 0.65 and 0.62e in the O_2–Pt_{13}-defective graphene and the O_2-free Pt_{13} nanoparticle systems, respectively. These results indicate that a strong linear relationship exists between the elongated O_2 bond lengths and the charge transferred to O_2.[15] The more activated the O_2 molecule is upon adsorption, indicated by the extent of the O–O bond distance elongation, the smaller the energy barrier required for dissociation.

Traditionally on flat metal surfaces, the more strongly O_2 is adsorbed, the more elongated the surface-bound O_2 bond is, which leads to the smaller the energy barrier for O_2 dissociation. This is demonstrated in previous investigations associated with flat metal surfaces that show a linear dependence between the O_2 adsorption energy and the O_2 dissociation barrier.[52] However, this trend shown on flat metal surfaces is contradictory to the relatively weaker O_2 adsorption energy (−2.30 eV) yet smaller O_2

dx.doi.org/10.1021/jp210796e | J. Phys. Chem. C 2012, 116, 3653–3660

Table 1. O−O Bond Lengths, Activation Energies of O_2 Dissociation (E_a),[a] and Pt−O and Pt−OH Bond Lengths of the Free Pt_{13} Nanoparticle (Pt_{13}) and Pt_{13}-Defective Graphene Systems (Pt_{13}/G) of Direct and Series Pathways[b]

	O−O (Å)			E_a (eV)		Pt−O (Å)			Pt−OH (Å)		
	direct		series	direct		direct		series	direct		
	Pt_{13}	Pt_{13}/G	Pt_{13}/G	Pt_{13}	Pt_{13}/G	Pt_{13}	Pt_{13}/G	Pt_{13}/G	Pt_{13}	Pt_{13}/G	series
step 1	1.23	1.23	1.23								
step 2	1.40	1.44	1.38	0.37	0.16	1.96*	1.93*	2.04*			
step 3	4.47	3.79	1.48			1.77*	1.78*	1.94			
step 4	4.57	3.49	3.58			1.77	1.79	1.77	1.92	1.93	1.94
step 5						1.77	1.78	1.77			
step 6									1.93	1.93	1.94

[a] E_a is calculated between steps 2 and 3. [b] Steps 1−6 correspond to images of Figure 3 and 4 (*indicates average lengths with ± less than 0.007 Å).

dissociation barrier energy on the Pt_{13}-defective graphene compared to those (adsorption energy of −3.92 eV)[15] on the free Pt_{13} nanoparticle. This is partly because, unlike flat metal surfaces, the stability of the O_2-free Pt_{13} system may be attributed to a significant geometry distortion of the free Pt_{13} nanoparticle upon O_2 adsorption. This can be further validated by examining the O_2 adsorption energy (i.e., −1.14 eV) on a fixed free Pt_{13} nanoparticle.[15]

Despite the stronger O_2 adsorption energy on the free Pt_{13} nanoparticle compared to that of the Pt_{13}-defective graphene, the O_2 molecule is more activated on the Pt_{13}-defective graphene as indicated by the O−O bond lengths of adsorbed O_2, which lowers the O_2 dissociation barrier energy compared to the unsupported system. However, the magnitude of difference in the degree of activated O_2 between the supported and unsupported Pt_{13} nanoparticles is small in terms of the elongated O−O bond and extent of charge transfer. Another important factor that may in part aid in explaining the difference in the O_2 dissociation barrier energy is the degree of relaxation associated with the free Pt_{13} nanoparticles. Upon O_2 adsorption, the overall change of the Pt atomic positions (i.e., defined as sum of the Pt atom diplacements after geometry optimization) of the unsupported and supported systems are 0.038 Å and 0.014 Å, respectively. This indicates that the number of degrees of freedom of the free Pt_{13} nanoparticle is greater than the supported Pt_{13} nanoparticle, which allows reconfiguration of the free particle upon O_2 adsorption. The higher number of degrees of freedom of the free Pt_{13} nanoparticle leads to the more stable adsorbed O_2 configuration, but less stable configuration of the transition state of O_2 dissociation. Although the comparison of the O_2 dissociation barrier energies indicate that the defective graphene support may be beneficial for lowering the O_2 dissociation barrier energy compared to the unsupported system, it may not influence the overall ORR since the rate-limiting step lies in the last proton/electron transfer and H_2O desorption step (i.e., steps 6 → 7 in Figure 3).

The lower energy barrier of the rate-limiting step for the supported Pt_{13} nanoparticle compared to the unsupported system potentially resulting in faster kinetics may be interpreted in terms of the d-band center shift. For transition metals, the position of the d-band center is a good measure of the relative reactivity of a given surface.[53,54] An upshift of the d-band center closer to the Fermi level (E_F) causes the antibonding orbitals of a catalytic surface to shift higher, potentially making them more difficult to fill, thereby leading to a stronger binding interaction between the adsorbate and surface. The d-band centers of defective graphene-supported Pt_{13} nanoparticle and free Pt_{13} nanoparticle are −1.98 and −1.89 eV, respectively. This is consistent with a previous DFT calculation[26] showing −2.05 and −1.71 eV, respectively, for Pt_{13}-defective graphene and free Pt_{13} in a shape of icosahedrons (which is different from our distorted cuboctahedron shape of Pt_{13}). In the case of the supported Pt_{13}, the d-band center is downshifted farther from E_F because of the defective graphene support. The relatively weaker interaction of the ORR intermediates with the supported Pt_{13} nanoparticle compared to that of the free Pt_{13} nanoparticle can be understood by the farther d-band center position from E_F, which results in the lower energy barrier for the rate-limiting step (i.e., step 6 → 7 in Figure 3) leading to relatively faster kinetics.

Series Pathway of ORR on Pt_{13}-Defective Graphene. A series two-electron pathway of ORR on defective graphene-supported Pt_{13} nanoparticles has also been investigated based on the direct pathway by replacing eq 5 and 6 by eq 10 and 11, respectively.

$$O_2^* + (H^+ + e^-) \rightarrow HOO^* \quad (10)$$

$$HOO^* \rightarrow O^* + OH^* \quad (11)$$

As discussed previously, while an addition of atomic hydrogen to the bridge O_2 adsorption configuration leads to dissociation of the O−O bond (Figure 2A), an addition of atomic hydrogen to the atop O_2 adsorption configuration forms HOO* species as shown in Figure 2B. An atop O_2 adsorption configuration (i.e., step 2 in Figure 4) is thus likely to proceed via the series pathway.[23] This is a major difference between the direct and series pathways for ORR, occurring at steps 2 and 3. The remaining steps 4−7 may be interchangeable between the direct and series pathways.

At zero electrode potential (i.e., U = 0 V), the series pathway is overall highly exothermic. By shifting the potential to the equilibrium electrode potential (i.e., U = 1.23 V), as in the direct pathway, the series pathway also shows that all of the four proton/electron-transfer steps are energetically uphill. The series ORR pathway on Pt(111)[2] has showed similar behavior at the HOO* formation step as shown in our study in that this reaction is endothermic at between steps 2 and 3. Under a high oxygen coverage of 0.5 ML, both O_2 adsorption and HOO* formation on Pt(111) are endothermic at the equilibrium electrode potential.[2]

A remarkable difference between the direct and series pathways occurs at steps 2 and 3 and is associated with the geometric stability of the HOO* intermediate species at step 3. Thus, additional geometry configurations of the HOO* intermediate species are examined with their minimum energy barriers between steps 2 and 3 in the series pathway predicted

dx.doi.org/10.1021/jp210796e | J. Phys. Chem. C 2012, 116, 3653−3660

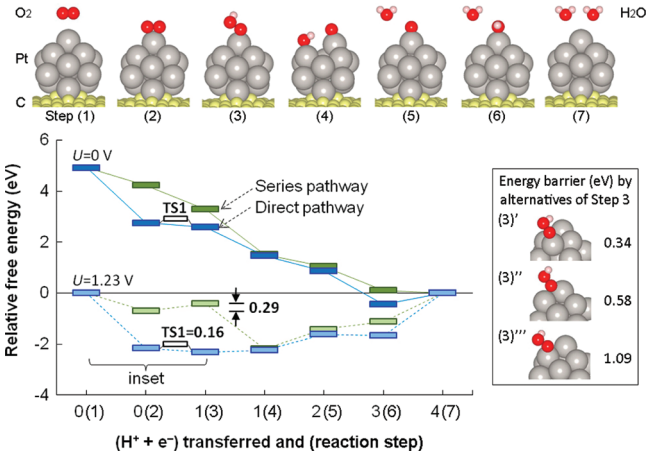

Figure 4. Free energy diagram for oxygen reduction through a direct four-electron (markers in blue) and a series two-electron (markers in green) pathway on defective graphene-supported Pt_{13} nanoparticles. Solid and dashed lines represent reactions at zero cell potential (i.e., U = 0 V) and the equilibrium potential (i.e., U = 1.23 V), respectively. Images of steps 1−2, 2−4, and 4−7 correspond to eqs 4, 10−11, and 7−9, respectively (a series two-electron pathway). Gas-phase species (e.g., O_2, H_2O, and H_2) are separately calculated and protons in the gas-phase are omitted in the images. TS 1 represents free energies of activation for O_2 dissociation on the supported Pt_{13} nanoparticles. The inset shows alternative intermediates (i.e., less stable) of steps 3′, 3″, and 3‴ of the series pathway at the equilibrium potential.

at the equilibrium electrode potential as shown in the inset of Figure 4. The O_2 dissociation barrier energy (TS1) of 0.16 eV in the direct pathway is lower than the minimum energy barrier of 0.29 eV between steps 2 and 3 of the series pathway, indicating that the direct pathway in which O_2 dissociates first is initially preferred compared to the HOO* species formation in the ORR pathway. This is an interesting finding compared to previous studies of ORR pathways on Pt(111)[3] and Pt clusters[19,24,55] approximating flat Pt surfaces, which have proposed that the HOO* species might be an intermediate for the initial proton transfer step. Among these previous studies, Wang and Balbuena[3] conducted ab initio molecular dynamics simulations of oxygen reduction on Pt(111) and suggested that the dissociation of adsorbed O_2* on Pt(111) may have a higher activation energy than that of the formation of the HOO* intermediate species, concluding that the HOO* formation may be an initial ORR step. This may be, however, because of a preferred O_2 adsorption configuration, which is a canted O−O structure at an atop-bridge site on flat Pt surfaces. In the work of Wang and Balbuena,[3] they showed that O_2 binds on Pt(111) in a canted HOO* configuration in both cases where a hydrated proton interacts with O_2 before or after O_2 adsorbs onto the surface. On the other hand, the canted O−O adsorption configuration is not the most stable adsorption configuration on Pt_{13} nanoparticles as extensively examined in our previous study.[15] Instead, because of highly undercoordinated Pt atoms of Pt_{13} nanoparticles, the bridge site for O_2 adsorption on the supported Pt_{13} nanoparticle (e.g., Figure 3B, step 2) may become more active in order to stabilize adsorbed O_2^*, which consequently results in strongly activated O_2^* species that lowers the O_2 dissociation barrier (e.g., TS1 in Figure 3 and 4).

As shown in Table 1, upon O_2 adsorption on the supported Pt_{13} nanoparticles, O_2 is activated by charge transferred from Pt atoms,[15] resulting in elongated O−O bond lengths of 1.38 and 1.44 Å from a gas-phase O_2 length of 1.23 Å at the atop (e.g., step 2 of the series pathway) and bridge (e.g., step 2 of the direct pathway) modes, respectively. This is consistent with their O_2 adsorption strength of −0.78 and −2.30 eV at the atop and bridge modes of the supported Pt_{13} nanoparticles, respectively,[15] in which the stronger O_2 adsorption leads to the more activated (i.e., the more elongated) O_2* species. The HOO* intermediate species of the series pathway (i.e., step 3) is likely to be a decomposition precursor as indicated by an elongated O−O bond distance of 1.48 Å and a shortened Pt−O bond distance of 1.94 Å compared to the adsorbed O_2* intermediate of step 2, which agrees with Wang and Balbuena.[3] This activated HOO* species decomposes to adsorbed O* and HO* species with its activation barrier small (i.e., 0.06 eV) according to previous DFT studies.[3,24] The reduction of HOO* may lead to H_2O by the formation of hydrogen peroxide ($H_2O_2^*$) intermediate (i.e., a series pathway)[3,21,55] or by directly forming H_2O and adsorbed O*.[2,3,55] Although the former was suggested to be the lower energy pathway,[55] it has generally been accepted that the $H_2O_2^*$ intermediate is unstable and thus readily dissociates homolytically into HO* + HO* species.[3,21] Our preliminary geometry optimization of the HOO-free Pt_{13} cluster with the addition of a H atom also shows that the latter is more likely to occur rather than the formation of an $H_2O_2^*$ species (Supporting Information, Figure S4). Thus, the remaining oxygen reduction steps after the formation of the HOO* intermediate species were determined and shown as steps 4−7 in Figure 4.

It should be noted that other important factors affecting the ORR pathways but not considered in this study may include the effect of water molecules and oxygen coverage on the stability of the ORR intermediates. Because of the polarity of HO* and HOO* species, they will interact more strongly with water molecules adsorbed on the Pt surface and will be further stabilized relatively, compared to O* species,[39] which might alter the ORR pathways suggested. The degree of oxygen coverage on the Pt_{13} nanoparticle surface will also affect the binding energies and free energy changes for ORR intermediates.[2] With an oxygen coverage of 0.5 ML, for example, O_2 requires a higher energy of dissociation,[2] which will ultimately influence the mechanism of oxygen reduction. Lastly, we have compared the ORR of the defective graphene-supported Pt_{13} nanoparticle with that of the free Pt_{13} nanoparticle to theoretically demonstrate the effect of the support on the ORR. However, it may not be appropriate to directly compare the results of the ORR of the supported Pt_{13} nanoparticle with those of flat Pt metal surfaces. For example, the overpotential of the supported Pt_{13} nanoparticle (i.e., ranging from 0.69 to 1.68 eV) is shown higher than the theoretically and experimentally observed overpotential (~0.45 eV)[2,56] of Pt(111). This is, however, because of the high reactivity of the Pt_{13} nanoparticle and monovacancy defect site of graphene employed in this study. If may be possible that larger Pt nanoparticles (i.e., > Pt_{13}) are less reactive than the smaller nanoparticle cluster examined in the current work, thereby leading to potentially lower overpotentials. Further work that examines the size effect on reactivity will aid in determining the possibly tunability of these composite nanostructures.

Electronic Properties. Figure 5A displays the excess Bader charge of each component (defective graphene, Pt_{13}, and adsorbates (O_2, OOH, O, or OH)) of the Pt_{13}-defective graphene and free Pt_{13} systems. Negative and positive excess charges represent charge depletion and accumulation, respectively. In all of the cases, it is clear that charge is transferred from the Pt_{13} nanoparticle to both defective graphene and the adsorbates.

dx.doi.org/10.1021/jp210796e | J. Phys. Chem. C 2012, 116, 3653−3660

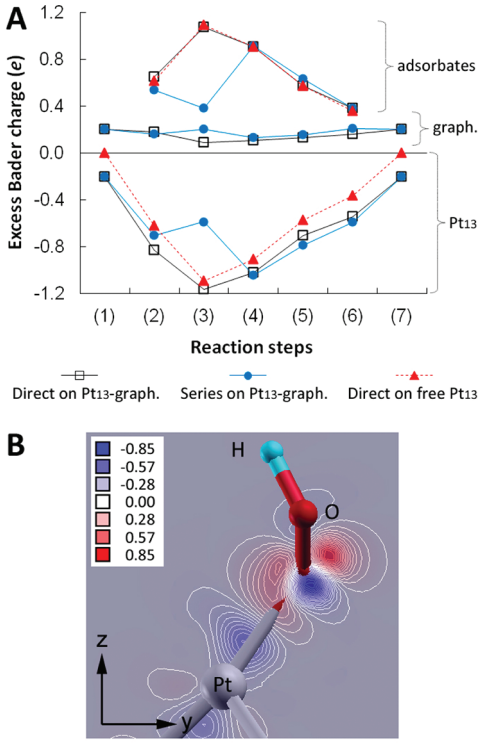

Figure 5. (A) Excess Bader charges (in units of e) of defective graphene (graph.), Pt_{13}, and adsorbates (O_2, OOH, O, or OH) of the Pt_{13}-defective graphene and free Pt_{13} systems depending on the direct and series oxygen reduction pathways. (B) Charge difference density ($\Delta n(\mathbf{r})$ in units of $e/Å^3$) of HOO* species (step 3) in the series pathway) showing the top part of Figure 2B (right).

Relatively strong charge depletion on Pt_{13} nanoparticle occurs at both interfaces of Pt_{13}/defective graphene and Pt_{13}/O_2 as shown in previous studies.[15,57] A significant difference between the direct and series pathways on the Pt_{13}-defective graphene systems is observed at step 3, where an HOO* intermediate species is formed in the series pathway. The relatively weaker interaction of the HOO* intermediate species with the supported Pt_{13} nanoparticle is responsible for both the decreased charge depletion on the Pt_{13} and decreased charge accumulation on the adsorbate. Between the direct pathways of the supported and unsupported Pt_{13} nanoparticles, the amount of charge transferred to the adsorbates is similar in both cases, but less charge depletion is observed on the unsupported Pt_{13} nanoparticle because of the absence of defective graphene that aids in depleting the charge of the Pt_{13} nanoparticle. Defective graphene shows similar charge accumulation between the direct and series pathways of the Pt_{13}-defective graphene system, which is not remarkably affected by adsorption. Figure 5B shows the charge difference density of the HOO* intermediate species (step 3) in the series pathway. Upon adsorption of HOO species, there is a charge depletion (in blue) from the vicinity of the top Pt atom and accumulation (in red) at the oxygen atoms. The charge difference density plot may not accurately describe the total amount of charge depleted and accumulated because of its known limitations, especially when adsorbates are significantly distorted upon adsorption[14,15] (i.e., charge densities of separated constitutes of an optimized system examined from the optimized composite system, not from their optimized gas-phase structures). For example, the magnitude of charge depletion of an Al nanoparticle upon adsorption on defective graphene was underestimated due to a significant geometry expansion of the Al nanoparticle.[14] Despite this limitation, Figure 5B clearly shows that the charge is transferred from the Pt atom to the HOO* species as discussed previously in the Bader charge analyses.

4. CONCLUSIONS

The current study has demonstrated theoretically that defective graphene used as a support structure may be used to enhance the catalytic activity of Pt_{13} nanoparticles. Comparing the free versus supported nanoparticle systems, the defective graphene support lowers the O_2 dissociation activation energy from 0.37 to 0.16 eV by promoting charge transfer from Pt atoms to O_2 and limiting the degree of relaxation of Pt_{13} nanoparticle, and also decreases the energy barrier of the rate-limiting step by reducing the stability of the HO* intermediate species. An additional benefit of the graphene support is its ability to anchor Pt nanoparticles to prevent sintering of the catalyst.

The ORR mechanisms via both the direct four-electron and series two-electron pathways have been investigated and compared. Both pathways show that at the equilibrium electrode potential (i.e., U = 1.23 V) all of the four proton/electron-transfer reactions are endothermic. A major difference between the two pathways examined occurs at the initial ORR step where O_2 adsorbs and either dissociates into O* + O* species (i.e., the direct pathway) or forms the HOO* intermediate species (i.e., the series pathway). By comparing O_2 dissociation activation energy (0.16 eV) and the minimum energy barrier for HOO* formation (0.29 eV), it has been found that the direct pathway is preferred at the initial step of the ORR pathway. The HOO* intermediate species in the series pathway is likely to be a decomposition precursor that decomposes to O* and HO* species. Following this step, three additional proton/electron-transfer steps lead to the formation of two water molecules, which may be interchangeable with the direct pathway. Lastly, upon adsorption of the ORR intermediate species on Pt_{13}-defective graphene, the Pt_{13} nanoparticle serves as a charge donor to both defective graphene and the intermediate species.

■ ASSOCIATED CONTENT

Ⓢ Supporting Information

Details of computational methodology including neutrally charged oxygen adsorbates, justification of fixing graphene surface, and free energy calculations, free energy diagram for simple oxygen reduction over bridge and atop sites of free Pt_{13} nanoparticles, and geometry optimization of H + HOO* adsorbed on free Pt_{13} nanoparticles. These materials are available free of charge via the Internet at http://pubs.acs.org.

■ AUTHOR INFORMATION

Corresponding Author

*E-mail: wilcoxj@stanford.edu. Phone: (650) 724-9449. Fax: (650) 725-2099.

■ ACKNOWLEDGMENTS

This material is based upon work supported by the Center on Nanostructuring for Efficient Energy Conversion (CNEEC) at Stanford University, an Energy Frontier Research Center funded by the U.S. Department of Energy, Office of Science, Office of Basic Energy Sciences under Award Number DE-SC0001060. The computational resources were supported by the National Science Foundation through TeraGrid resources

provided by TACC. Authors greatly appreciate useful comments and discussion with Professors Jens K. Nørskov and Thomas Francisco Jaramillo at Stanford University.

REFERENCES

(1) Yeager, E. *Electrochim. Acta* **1984**, *29*, 1527.
(2) Nørskov, J. K.; Rossmeisl, J.; Logadottir, A.; Lindqvist, L.; Kitchin, J. R.; Bligaard, T.; Jónsson, H. *J. Phys. Chem. B* **2004**, *108*, 17886.
(3) Wang, Y. X.; Balbuena, P. B. *J. Phys. Chem. B* **2005**, *109*, 14896.
(4) Calvo, S. R.; Balbuena, P. B. *Surf. Sci.* **2007**, *601*, 165.
(5) Litster, S.; McLean, G. *J. Power Sources* **2004**, *130*, 61.
(6) Wang, J. X.; Inada, H.; Wu, L.; Zhu, Y.; Choi, Y.; Liu, P.; Zhou, W.-P.; Adzic, R. R. *J. Am. Chem. Soc.* **2009**, *131*, 17298.
(7) Kou, R.; Shao, Y.; Wang, D.; Engelhard, M. H.; Kwak, J. H.; Wang, J.; Viswanathan, V. V.; Wang, C.; Lin, Y.; Wang, Y.; Aksay, I. A.; Liu, J. *Electrochem. Commun.* **2009**, *11*, 954.
(8) Seger, B.; Kamat, P. V. *J. Phys. Chem. C* **2009**, *113*, 7990.
(9) Rao, C. V.; Reddy, A. L. M.; Ishikawa, Y.; Ajayan, P. M. *Carbon* **2011**, *49*, 931.
(10) Seo, M. H.; Choi, S. M.; Kim, H. J.; Kim, W. B. *Electrochem. Commun.* **2011**, *13*, 182.
(11) Yoo, E.; Okata, T.; Akita, T.; Kohyama, M.; Nakamura, J.; Honma, I. *Nano Lett.* **2009**, *9*, 2255.
(12) Shao, Y.; Zhang, S.; Wang, C.; Nie, Z.; Liu, J.; Wang, Y.; Lin, Y. *J. Power Sources* **2011**, *195*, 4600.
(13) Wang, M.-x.; Xu, F.; Sun, H.-f.; Liu, Q.; Artyushkova, K.; Stach, E. A.; Xie, J. *Electrochim. Acta* **2011**, *56*, 2566.
(14) Lim, D.-H.; Negreira, A. S.; Wilcox, J. *J. Phys. Chem. C* **2011**, *115*, 8961.
(15) Lim, D.-H.; Wilcox, J. *J. Phys. Chem. C* **2011**, *115*, 22742.
(16) Simon, P.; Gegotsi, Y. *Nat. Mater.* **2008**, *7*, 845.
(17) Hashimoto, A.; Suenaga, K.; Gloter, A.; Urita, K.; Iijima, S. *Nature* **2004**, *430*, 870.
(18) Coleman, V. A.; Knut, R.; Karis, O.; Grennberg, H.; Jansson, U.; Quinlan, R.; Holloway, B. C.; Sanyal, B.; Eriksson, O. *J. Phys. D: Appl. Phys.* **2008**, *41*, 062001.
(19) Tsuda, M.; Kasai, H. *J. Phys. Soc. Jpn.* **2007**, *76*, 024801.
(20) Marković, N. M.; Schmidt, T. J.; Stamenković, V.; Ross, P. N. *Fuel Cells* **2001**, *1*, 105.
(21) Lamas, E. J.; Balbuena, P. B. *J. Chem. Theory Comput.* **2006**, *2*, 1388.
(22) Adzic, R. *Electrocatalysis*; Wiley-VCH: New York, 1998.
(23) Yeager, E. *J. Electrochem. Soc.* **1981**, *128*, 160C.
(24) Sidik, R. A.; Anderson, A. B. *J. Electroanal. Chem.* **2002**, *528*, 69.
(25) Yamamoto, K.; Imaoka, T.; Chun, W.-J.; Enoki, O.; Katoh, H.; Takenaga, M.; Sonoi, A. *Nat. Chem.* **2009**, *1*, 397.
(26) Toyoda, E.; Jinnouchi, R.; Hatanaka, T.; Morimoto, Y.; Mitsuhara, K.; Visikovskiy, A.; Kido, Y. *J. Phys. Chem. C* **2011**, DOI: 10.1021/jp206360e.
(27) Kresse, G.; Hafner, J. *Phys. Rev. B* **1993**, *47*, 558.
(28) Kresse, G.; Hafner, J. *Phys. Rev. B* **1994**, *49*, 14251.
(29) Kresse, G.; Furthmüller, J. *Phys. Rev. B* **1996**, *54*, 11169.
(30) Kresse, G.; Furthmüller, J. *Comput. Mater. Sci.* **1996**, *6*, 15.
(31) Blöchl, P. E. *Phys. Rev. B* **1994**, *50*, 17953.
(32) Kresse, G.; Joubert, D. *Phys. Rev. B* **1999**, *59*, 1758.
(33) Perdew, J. P.; Burke, K.; Ernzerhof, M. *Phys. Rev. Lett.* **1996**, *377*, 3865.
(34) Monkhorst, H. J.; Pack, J. D. *Phys. Rev. B* **1976**, *13*, 5188.
(35) Methfessel, M.; Paxton, A. T. *Phys. Rev. B* **1989**, *40*, 3616.
(36) Sakurai, M.; Watanabe, K.; Sumiyama, K.; Suzuki, K. *J. Chem. Phys.* **1999**, *111*, 235.
(37) Lian, L.; Su, C. X.; Armentrout, P. B. *J. Chem. Phys.* **1992**, *97*, 4072.
(38) Henkelman, G.; Uberuaga, B. P.; Jonsson, H. *J. Chem. Phys.* **2000**, *113*, 9901.
(39) Rossmeisl, J.; Logadottir, A.; Nørskov, J. K. *Chem. Phys.* **2005**, *319*, 178.
(40) Peterson, A. A.; Abild-Pedersen, F.; Studt, F.; Rossmeisl, J.; Nørskov, J. K. *Energy Environ. Sci.* **2010**, *3*, 1311.
(41) Cramer, C. J. *Essentials of Computational Chemistry Theories and Models*, 2nd ed.; John Wiley & Sons, Ltd.: West Sussex, England, 2004.
(42) Bader, R. F. W. *Chem. Rev.* **1991**, *91*, 893.
(43) Henkelman Group, The University of Texas at Austin, http://theory.cm.utexas.edu/henkelman/research/bader/.
(44) Tang, W.; Sanville, E.; Henkelman, G. *J. Phys.: Condens. Matter* **2009**, *21*, 084204.
(45) Lin, X.; Ramer, N. J.; Rappe, A. M.; Hass, K. C.; Schneider, W. F.; Trout, B. L. *J. Phys. Chem. B* **2001**, *105*, 7739.
(46) Michaelides, A.; Hu, P. *J. Chem. Phys.* **2001**, *114*, 513.
(47) Koper, M. T. M.; Shubina, T. E.; van Santen, R. A. *J. Phys. Chem. B* **2002**, *106*, 686.
(48) Miller, D. J.; Öberg, H.; Näslund, L. Å.; Anniyev, T.; Ogasawara, H.; Pettersson, L. G. M.; Nilsson, A. *J. Chem. Phys.* **2010**, *133*, 224701.
(49) Sljivancanin, Z.; Hammer, B. *Surf. Sci.* **2002**, *515*, 235.
(50) Sha, Y.; Yu, T. H.; Merinov, B. V.; Shirvanian, P.; Goddard, W. A. III. *J. Phys. Chem. Lett.* **2011**, *2*, 572.
(51) Shan, B.; Kapur, N.; Hyun, J.; Wang, L.; Nicholas, J. B.; Cho, K. *J. Phys. Chem. C* **2009**, *113*, 710.
(52) Nørskov, J. K.; Bligaard, T.; Logadottir, A.; Bahn, S.; Hansen, L. B.; Bollinger, M.; Bengaard, H.; Hammer, B.; Sljivancanin, Z.; Mavrikakis, M.; Xu, Y.; Dahl, S.; Jacobsen, C. J. H. *J. Catal.* **2002**, *209*, 275.
(53) Hammer, B.; Nørskov, J. K. *Surf. Sci.* **1995**, *343*, 211.
(54) Hammer, B.; Nørskov, J. K. Theoretical Surface Science and Catalysis: Calculations and concepts. In *Advances in Catalysis*, Vol *45*; Academic Press Inc: San Diego, CA, 2000; Vol. *45*; pp 71.
(55) Anderson, A. B.; Albu, T. V. *J. Electrochem. Soc.* **2000**, *147*, 4229.
(56) Hoogers, G.; Thomsett, D. *CATTECH* **1999**, *3*, 106.
(57) Qi, L.; Qian, X. F.; Li, J. *Phys. Rev. Lett.* **2008**, *101*, 146101.